energies

Article

A Nonlinear Wind Turbine Wake Expansion Model Considering Atmospheric Stability and Ground Effects

Xing Xing Han [1,2], Tong Guang Wang [2], Xian Dong Ma [3], Chang Xu [1,*], Shi Feng Fu [4], Jin Meng Zhang [1], Fei Fei Xue [1] and Zhe Cheng [1]

[1] College of Renewable Energy, Hohai University, Changzhou, China
[2] College of Aeronautics, Nanjing University of Aeronautics and Astronautics, Nanjing, China
[3] School of Engineering, Lancaster University, Lancaster LA1 4YW, United Kingdom
[4] College of Electrical Energy and Power Engineering, Yangzhou University, Yangzhou, China
* Correspondence: zhuifengxu@hhu.edu.cn; Tel.: +86+13951792223

Abstract: This study investigates the influence of atmospheric stability and ground effects on wind turbine wake recovery, challenging the conventional linear relationship between turbulence intensity and wake expansion coefficient. Through comprehensive field measurements and numerical simulations, we demonstrate that the linear wake expansion assumption is invalid at far-wake locations under high turbulence conditions, primarily due to ground effects. We propose a novel nonlinear wake expansion model that incorporates both atmospheric stability and ground effects by introducing a logarithmic relationship between the wake expansion coefficient and turbulence intensity. Validation results reveal superior prediction accuracy of the proposed model compared to typical engineering wake models, with root mean square errors of wake wind speed predictions ranging from 0.04 to 0.063. This proposed model offers significant potential for optimizing wind farm layouts and enhancing overall wind energy production efficiency.

Keywords: wind turbine; nonlinear wake expansion model; atmospheric stability; ground effects

1. Introduction

Wind turbine wakes, characterized by reduced velocity and increased turbulence, significantly impact downstream turbine performance. These wakes are influenced by atmospheric conditions, ground effects, and turbine characteristics. Engineering wake models, crucial for wind farm design and operation, have evolved from simple linear models to more complex Gaussian models. However, most existing models assume a linear relationship between wake expansion and turbulence intensity, often neglecting the effects of atmospheric stability and ground interactions. This assumption may be invalid under high turbulence conditions or in far-wake regions, especially in unstable atmospheric states where ground effects become significant. There is a need for more sophisticated models that can accurately capture these complex wake behaviors.

Numerous wind tunnel [1-3] and field experiments [4-6] have demonstrated that atmospheric stability can significantly affect wind turbine wakes. Chamorro et al. [1] through analysis of wind tunnel experiment data, found that under stable conditions, larger vertical gradients in wind speed compared to neutral conditions could enhance turbulence intensity in the wake region and extend its influence. Zhang et al [3] in wind tunnel experiments, observed that under unstable conditions, higher turbulence intensity compared to neutral conditions promotes wake recovery, resulting in a reduction of wake losses by approximately 15% and an increase in maximum turbulence intensity by 20%. Currently, engineering wake models that consider the influence of atmospheric stability primarily include the improved Jensen model by Peña et al. [7] and the wake model proposed by Cheng et al. [8]. The improved Jensen model predicts a wake profile resembling

Citation: To be added by editorial staff during production.

Academic Editor: Firstname Lastname

Received: date
Revised: date
Accepted: date
Published: date

a "top-hat", which differs significantly from the measured Gaussian-like distribution shape. The Cheng model [8] has only been validated using numerical simulation results and lacks validation with field measurements, thus its reliability requires further investigation.

Ground effects on wind turbine wakes are multifaceted and significant. The ground surface plays a crucial role in several aspects of the wake behavior. These include (1) Ground-induced turbulence and anisotropy: the ground significantly contributes to turbulence in the lower atmosphere. Under neutral conditions, larger ground roughness increases turbulence intensity, accelerating wake recovery [9]. This ground-induced turbulence is also anisotropic, causing disparities between vertical and horizontal wake recovery rates [10]. (2) Wake profile shearing: the presence of the ground causes shearing of the wake profiles, introducing additional complexity to wakes. Several three-dimensional wake models have been proposed in recent years [11-13]. (3) Momentum interaction: at far-wake region, the ground interaction of the wake impedes wake expansion toward the surface and may break down the linear wake expansion assumption [14]. At near and intermediate wake locations (approximately 3-5 rotor diameters downstream), the vertical distribution of the streamwise velocity deficit exhibits symmetry around the hub height. However, this symmetry breaks down in the far-wake region [15]. For simplicity, we focus on examining how ground effects influence wake expansion in this study.

This study addresses the above issues using numerical simulations to investigate the inhibitory effect of the ground on the wake expansion coefficient of wind turbines. A nonlinear wake expansion model that incorporates atmospheric stability and ground effects is proposed based on both measured data and relevant numerical simulation results. The remainder of this paper is organized as follows. The effects of ground and atmospheric stability on wind turbine wake expansion are studied in Section 2. The improved Jensen wake model and several typical models are introduced in Section 3. The nonlinear wake expansion model based on the experimental and numerical results is proposed in Section 4 and validated in Section 5. The conclusions are presented in Section 6.

2. Effects of ground on the wind turbine wake expansion

2.1. FullRF turbulence model for wake modeling

The study applies the FullRF turbulence model [16] and the actuator disk model to simulate wind turbine wake, with the control equations adopted as:

$$\frac{\partial}{\partial x_i}(\rho U_i) = 0 \tag{1}$$

$$\frac{\partial}{\partial t}(\rho U_i) + \frac{\partial}{\partial x_j}(\rho U_i U_j) = -\frac{\partial p}{\partial x_i} + \frac{\partial}{\partial x_j}\left[(\mu + \mu_t)\left(\frac{\partial U_i}{\partial x_j} + \frac{\partial U_j}{\partial x_i}\right)\right] + S_{u,i} \tag{2}$$

$$\frac{\partial}{\partial t}(\rho\Theta) + \frac{\partial}{\partial x_i}(\rho U_i \Theta) = \frac{\partial}{\partial x_i}\left[\left(\frac{\mu}{Pr} + \alpha_t\right)\frac{\partial \Theta}{\partial x_i}\right] \tag{3}$$

$$\frac{\partial}{\partial t}(\rho k) + \frac{\partial}{\partial x_i}(\rho U_i k) = \frac{\partial}{\partial x_j}\left[\left(\mu + \frac{\mu_t}{\sigma_k}\right)\frac{\partial k}{\partial x_j}\right] + \mathcal{P} + \mathcal{B} - \rho\varepsilon - S_{k,\mathrm{ASL}} \tag{4}$$

$$\frac{\partial}{\partial t}(\rho\varepsilon) + \frac{\partial}{\partial x_i}(\rho U_i \varepsilon) = \frac{\partial}{\partial x_j}\left[\left(\mu + \frac{\mu_t}{\sigma_\varepsilon}\right)\frac{\partial \varepsilon}{\partial x_j}\right] + (C_{\varepsilon 1}\mathcal{P} - \rho C_{\varepsilon 2}\varepsilon + C_{\varepsilon 3}\mathcal{B})\frac{\varepsilon}{k} + S_{\varepsilon,\mathrm{wake}} \tag{5}$$

where U_i and U_j represent the velocity components along the x_i and x_j axes respectively, *p* is pressure, μ is molecular viscosity, μ_t is the turbulent viscosity and $S_{u,i}$ is the momentum source term exerted by the wind turbine on the x_i axis. Θ is the potential temperature, $Pr = 0.9$ is the laminar Prandtl number, $\alpha_t \equiv \mu_t/Pr_t$ is the turbulent heat conductivity and $Pr_t \equiv \phi_h/\phi_m$ is the turbulent Prandtl number. The similarity functions ϕ_m and ϕ_h are described in Section 2.1.1. *k* is the turbulence kinetic energy (TKE), ε is the

TKE dissipation, $C_\mu = 0.033$, $\sigma_k = 1.0$, $\sigma_\varepsilon = 1.3$, $C_{\varepsilon 2} = 1.92$. The turbulent kinetic energy generation rate $\mathcal{P}$ due to the mean velocity gradient and the turbulent kinetic energy generation rate $\mathcal{B}$ due to the buoyancy force can be expressed under the Boussinesq assumption:

$$\mathcal{P} \equiv -\rho \overline{u_i' u_j'} \frac{\partial U_i}{\partial x_j} = \mu_t \left(\frac{\partial U_i}{\partial x_j} + \frac{\partial U_j}{\partial x_i} \right) \frac{\partial U_i}{\partial x_j} \tag{6}$$

$$\mathcal{B} \equiv \frac{g_j}{\Theta_0} \overline{u_j' \theta'} = -\frac{g_j}{\Theta_0} \frac{\mu_t}{Pr_t} \frac{\partial \Theta}{\partial x_j} \tag{7}$$

where g_j is the component of gravitational acceleration along the x_j axis.

This section uses the BEM method to simulate the wind turbine model. The Boundary Element Method (BEM) is a numerical computational technique used to solve partial differential equations, requiring discretization only on the boundary of the problem domain.

In the BEM-based actuator disk model, the rotor plane consists of N actuator lines, each of which is split into M element sections (Figure 1). The element section collects the local velocity and rotor speed Ω to calculate the element force, and applies this force to the neighboring cells of the element section. The reference velocity is first assessed from the disk-averaged velocity, and is then applied to evaluate the rotor speed.

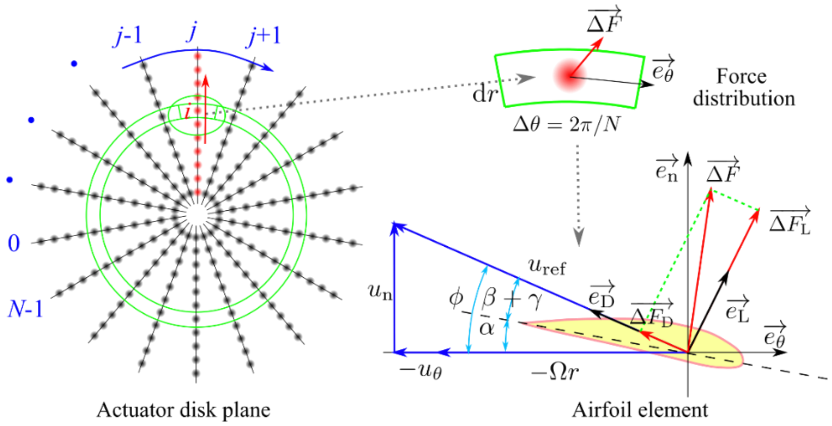

Figure 1. Mesh element and schematic diagram of forces of actuated disc model based on BEM.

By transforming the local velocity at the blade element into polar velocity components (Ωr, u_θ, and u_n), the force of the blade element is

$$\overrightarrow{\Delta F} = \rho \frac{Bc \Delta\theta \Delta r}{4\pi} \left(C_L \overrightarrow{e_L} + C_D \overrightarrow{e_D} \right) \left[u_n^2 + (\Omega r + u_\theta)^2 \right] \tag{8}$$

where B is the number of blades, c is the chord length, and Δr is the element section length. The drag coefficient of the element section, C_D, and its lift coefficient, C_L, which are functions of the attack angle α, are estimated from XFOIL [17] and then corrected by the three-dimensional rotational effects of the blades based on Du et al. [18]. According to Figure 1, $\alpha = \varphi - (\beta + \gamma)$, where $\varphi = \arctan [u_n/(\Omega r + u_\theta)]$ is the flow angle, β is the blade installation angle, and γ is the pitch angle.

The element force is distributed across neighboring cells. The force added to a cell is calculated by

$$\overrightarrow{\Delta F_{\text{cell}}} = \sum_{j=0}^{N-1} \sum_{i=0}^{M-1} \frac{1}{s^3 \pi^{3/2}} \exp\left(-\frac{s_{i,j}^2}{s^2} \right) \overrightarrow{\Delta F_{i,j}} f_i^{\text{tip}} f_i^{\text{hub}} \Delta V_{\text{cell}} \tag{9}$$

where $s_{i,j}$ is the distance of the i-th element to the cell and s is the cut-off length scale that takes a value between two and three cell sizes [19]. F_{tip} and F_{hub} are the Prandtl tip loss and hub loss functions [20]:

$$f_i^{\text{tip}} = \frac{2}{\pi} \arccos \left[\exp\left(\frac{B(R - r_i)}{2 r_i \sin \phi_i} \right) \right] \tag{10}$$

$$f_i^{\text{hub}} = \frac{2}{\pi}\arccos\left[\exp\left(\frac{B(r_i - R_{\text{hub}})}{2r_i \sin\phi_i}\right)\right] \tag{11}$$

where R is the rotor radius, R_{hub} is the hub radius, and r is the radial distance between the element and rotor center.

2.1.1 Turbulence Modeling

In the FullRF turbulence model, an TKE source term and the coefficient $C_{\varepsilon 3}$ are calibrated to keep flow homogeneity:

$$S_{k,\text{ASL}} = \left[\phi_m - \phi_\varepsilon - \zeta + \frac{C_\mu^{-1/2}\kappa^2}{\sigma_k}\frac{\zeta^2}{\phi_m}\left(\phi_k'' - \frac{\phi_k'\phi_m'}{\phi_m} + \frac{\phi_k'}{\zeta}\right)\right]\frac{u_*^3}{\kappa z} \tag{12}$$

$$C_{\varepsilon 3} = \frac{C_{\varepsilon 1}\phi_m - C_{\varepsilon 2}\phi_\varepsilon}{\zeta} + \frac{C_\mu^{-1/2}\kappa^2}{\sigma_\varepsilon}\frac{\phi_k}{\phi_m}\left(\frac{\zeta\phi_\varepsilon''}{\phi_\varepsilon} - \frac{\zeta\phi_\varepsilon'\phi_m'}{\phi_\varepsilon\phi_m} - \frac{\phi_\varepsilon'}{\phi_\varepsilon} + \frac{\phi_m'}{\phi_m} + \frac{1}{\zeta}\right) \tag{13}$$

where the similarity functions are

$$\phi_m(\zeta) = \begin{cases} (1-16\zeta)^{-1/4} & \zeta < 0 \\ (1+40\zeta)^{1/4} & 0 < \zeta \end{cases} \tag{14}$$

$$\phi_h(\zeta) = \begin{cases} 0.9(1-16\zeta)^{-1/2} & -2 < \zeta < 0 \\ 0.9(1+5\zeta)^{1/4} & 0 < \zeta < 1 \end{cases} \tag{15}$$

$$\phi_\varepsilon(\zeta) \equiv \frac{\kappa z}{u_*^3}\varepsilon = \begin{cases} 1-\zeta & \zeta < 0 \\ \phi_m - \zeta & \zeta > 0 \end{cases} \tag{16}$$

$$\phi_k(\zeta) \equiv \frac{\sqrt{C_\mu}}{u_*^2}k = \sqrt{\frac{\phi_\varepsilon(\zeta)}{\phi_m(\zeta)}} \tag{17}$$

The source term $S_{\varepsilon,\text{wake}}$ for turbulent kinetic energy dissipation is applied within a cylindrical region downstream of the wind turbine with a distance of 0.25 times the rotor diameter, aiming to correct the issue of rapid wake recovery induced by the $k-\varepsilon$ standard turbulence model.

$$S_{\varepsilon,\text{wake}} = \rho C_{\varepsilon 4}\frac{\mathcal{P}^2}{\rho k} \tag{18}$$

in which $C_{\varepsilon 4} = 0.37$.

In addition, Alinot and Masson [21], M.P. van der Laan [22], proposed two near-surface turbulence models based on the Businger-Dyer similarity function, which are referred to as the AM model and the Laan mode. Section 2.2.3 will study the effects of atmospheric stability on wind turbine wake for the aforementioned models.

2.1.2 Boundary Conditions

The boundary conditions consistent with similarity functions are applied to model the atmospheric boundary stratification. The inlet profiles of wind speed, potential temperature, TKE, and its dissipation are given by

$$U(z) = \int_{z_0}^{z}\frac{u_*}{\kappa z}\phi_m\left(\frac{z}{L}\right)\mathrm{d}z \tag{19}$$

$$\Theta(z) = \Theta_0 + \int_{z_0}^{z}\frac{\theta_*}{\kappa z}\phi_h\left(\frac{z}{L}\right)\mathrm{d}z \tag{20}$$

$$\varepsilon(z) = \frac{u_*^3}{\kappa z}\phi_\varepsilon\left(\frac{z}{L}\right) \tag{21}$$

$$k(z) = \frac{u_*^2}{\sqrt{C_\mu}}\phi_k\left(\frac{z}{L}\right) \tag{22}$$

The vertical profiles of wind speed are estimated in numerical integration. Zero gradients of U, Θ, ε, and k are applied at the outlet. For the top boundary, the upstream flow properties are maintained constant. The left and right sides of the computational domain are symmetrical. The near-wall treatment of Temel et al. [23] is implemented in the near-ground region to calculate the turbulent dissipation rate and TKE production $G_{k,p}$ owing to shear and buoyancy:

$$\varepsilon_p = \frac{u_{*k}^3}{\kappa z_p}\phi_{\varepsilon,p} \tag{23}$$

$$G_{k,p} = \frac{\tau_w^2}{\rho\kappa u_{*k}(z_p + z_0)} - \frac{\theta_*|g|}{\Theta_0(z_p + z_0)} \tag{24}$$

where the subscript p denotes the first cell center above the ground, the equivalent friction wind speed is $u_{*k} = C_\mu^{0.25}\phi_{k,p}^{-0.5}k_p^{0.5}$, and the wall shear stress is $\tau_w = \mu_{t,p}(\mathrm{d}U/\mathrm{d}z)$. The eddy viscosity $\mu_{t,p}$ and the turbulent heat conductivity are imposed at the first cell center above the ground as [24]:

$$\mu_{t,p} = \frac{u_{*k} z_p}{\displaystyle\int_{z_0}^{z_p} \frac{1}{\kappa z}\phi_m\left(\frac{z}{L}\right)\mathrm{d}z} - \mu \tag{25}$$

$$\alpha_{t,p} = \mu_{t,p}\phi_{m,p}/\phi_{h,p} - \mu/Pr \tag{26}$$

2.2. Model validation

2.2.1 Test Case

For the validation of the FullRF model, the scenarios outlined in reference [16] only involved wind turbines with capacities below 1 MW and lacked examinations under neutral and unstable atmospheric conditions. In this study, wake measurement data from the Jingbian wind farm [4] are used to further substantiate the FullRF model. Figure 2 shows the wind farm's topography and the layout of wind turbines; the X and Y axes are oriented towards the east and north, respectively. The southern region of the wind farm, characterized by a valley with complex topography, contrasts with the relatively flat northern expanse. The experimental wind turbine #14 has a rated capacity of 2 MW, rotor diameter of 90 m, and hub height of 67 m, and is situated in a transitional zone between the valley and flat terrain. Consequently, wake measurements were executed using masts M1 and M3, positioned to the south and north of turbine #14, at horizontal distances approximately 1.45 times and 2.15 times the rotor diameter, respectively. The masts were equipped with Thies First Class cup anemometers, temperature and wind direction sensors, and Metek 3D ultrasonic anemometers, which provided wind speed and temperature data at a frequency of 35 Hz. The study included approximately 190 days of valid acoustic measurements and an additional 310 days of supplementary data, including non-acoustic mast data and operational information from the wind farm. Since the atmospheric boundary layer classification relies on acoustic measurements, this study uses 190 days of data for analysis.

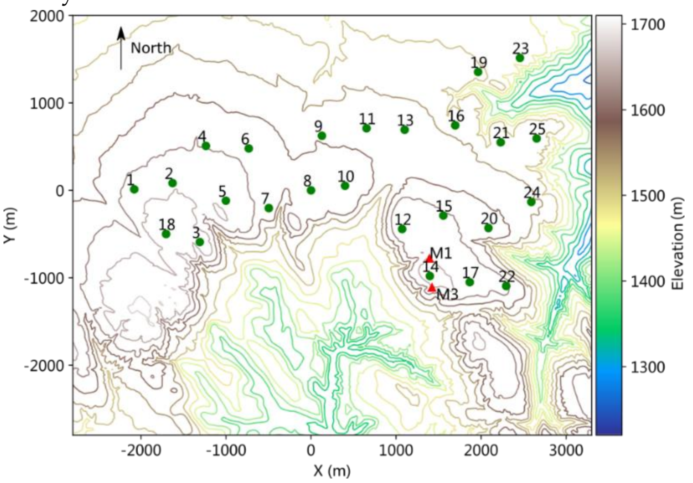

Figure 2. Complex terrains and layout of the Jingbian wind farm.

Masts were strategically positioned on both the north and south sides of wind turbine #14, as shown in Figure 3. This setup enabled the acquisition of the wake wind velocity and turbulence intensity profiles at axial distances of 1.45*D* and 2.15*D* behind the turbine. Given that wind turbines are typically spaced more than 4*D* apart, calculations of wind resources and forecasts of wind power are primarily concerned with the far-wake region of turbines. Additionally, the nacelle wind speed, when combined with the nacelle transfer function, provides a partial estimation of the wind speed at the turbine. To augment this data, an experimental setup involving additional turbine #12 was introduced near the M1 mast to capture the wake profile at a further axial distance of 5*D*, as depicted in Figure 4.

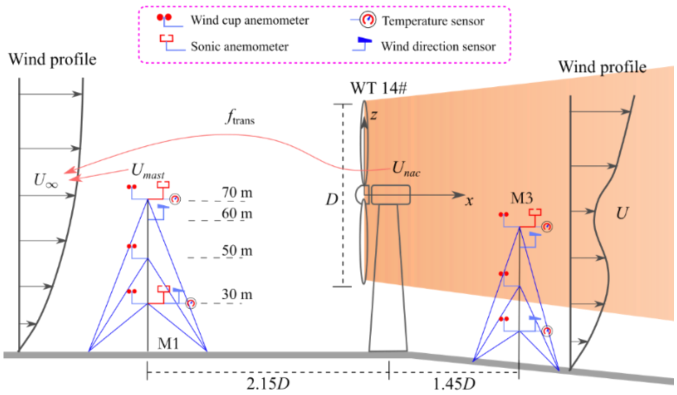

Figure 3. Wake measurements for downstream distances of 1.45*D* and 2.15*D*. *D* represents the rotor diameter of the wind turbine, same as above for the subsequent text.

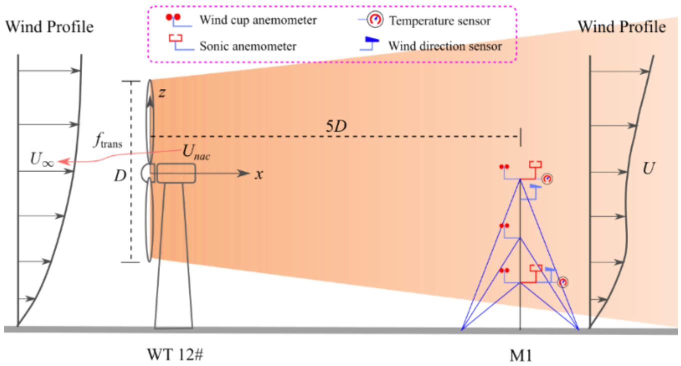

Figure 4. Wake measurements for downstream distances of 5*D*.

The wind speed of the hub corresponding to the wake measurement data of the wind turbine is 6 m/s, the atmospheric roughness is 0.05 m. The flow parameters corresponding to each stability degree are listed in Table 1, where "Classical" stands for the Businger-Dyer similarity functions [25, 26].

Table 1. Inflow parameters for wake simulations of Haizhuang 2WM wind turbine.

Atmosphere stability	*L* (m)	Measured I_u (%)	CFD u^* (m/s)		CFD *Iu* (%)	
			Classical	FullRF	Classical	FullRF
Unstable	-30	17.6	0.425		22.8	
Netural	∞	11.6	0.333		10.6	
Stable	30	7.8	0.131	0.208	4	9

2.2.2 Computational Domain, Meshing and Solver Settings

The calculation domains of the wind turbine wake simulation are 20*D*, 10*D*, and 10*D*, respectively (Figure 5). To effectively incorporate the wind turbine source term into the computational cells and capture the wake structure, the mesh of the computational domain is segmented into four refinement levels. A cell at level *i* can be subdivided into four cells at level *i*+1. The background grid with refinement level 0 contains 100 (long) × 60 (wide) × 60 (high) cells. The background grid is uniformly divided in the horizontal plane, and refined near the ground in the height direction, and the height of the grid is set to 7.38z_0 [27]. The grid refinement level in the region of the wind turbine actuator is set to 3, distributing approximately 80 grid nodes across the diameter and length of the turbine [28]. The actuator disk regions 5*D* and 10*D* downstream are refined to levels 2 and 3, respectively, to ensure detailed capture of the wake structures. The computational domain contains approximately 1.6 million cells. In this study, turbulence models are implemented in OpenFOAM [29] using the finite volume method. A large time-step transient solver using the PIMPLE algorithm is applied to simulate wakes of wind turbines. During the iteration, the source terms S_u and $S_{\varepsilon,wake}$ are modeled based on local flow information via user-specified finite volume options. For temporal and spatial discretization in the simulations, a second-order backward difference scheme and a second-order central difference scheme are applied, respectively.

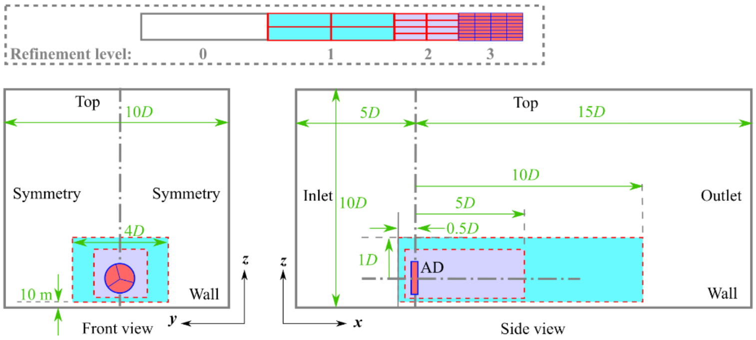

Figure 5. Sketch of computational domain and meshing.

2.2.3 Results

Figure 6 presents a comparison between the relative wind speeds predicted by the wake model at various axial distances and the corresponding empirical measurements. Here, FullRF denotes the utilization of the FullRF turbulence model coupled with the BEM-based actuator disk model, whereas FullRF-CT refers to the adoption of the FullRF turbulence model integrated with an actuator disk model that employs thrust coefficients.

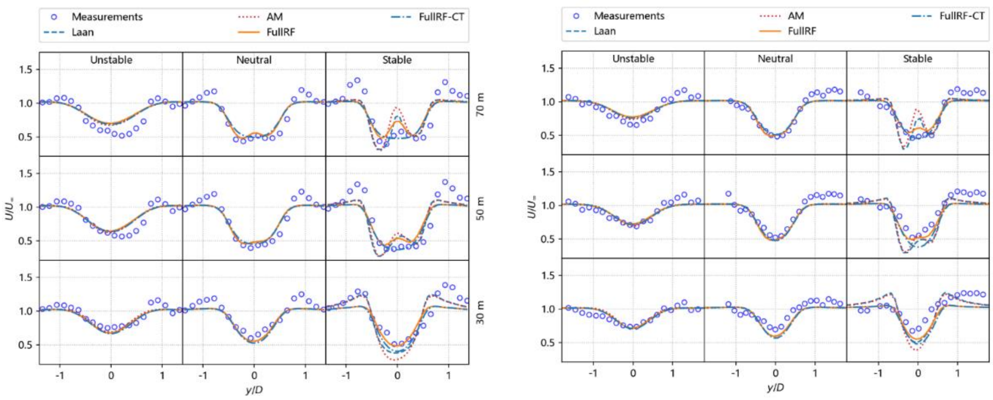

(a) (b)

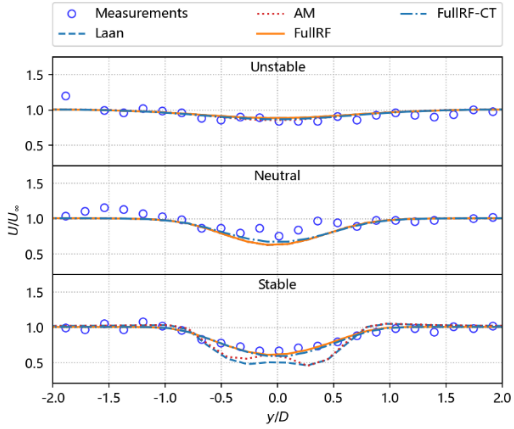

(c)

Figure 6. Relative wind speed in the wake of Haizhuang wind turbine: (a) 1.45D; (b) 2.15D; (c) 5D.

Figure 7 illustrates the correlation between the root mean square error (RMSE) of wind speed at different axial distances. Since the actuator disk model based on the thrust coefficient does not add a momentum source term to the nacelle position, the actuating disk resembles a ring shape, forming a bimodal phenomenon when the wind speed decreases at a hub height of 1.45*D* after the wind wheel. Compared with the AM model and the Laan model, the wake predicted by the FullRF and FullRF-CT models has a lower RMSE relative to the wind speed, which has a good agreement with the measured values. Under stable conditions, the AM model and the Laan models significantly overestimate the wind speed loss in the wake region, and overestimate the wake loss by approximately 40% at 5*D*, and the corresponding RMSE is maintained at approximately 0.15. The RMSE of the wake predicted by the FullRF and FullRF-CT models is only about 0.7 on average, which effectively improves the phenomenon of overestimating the wind speed loss caused by the Businger-Dyer similarity functions. Under unstable conditions, the turbulence intensity of the reference flow provided by the model is 22.8%, which is greater than the measured value of 18%, which accelerates the recovery speed of the wake in the simulation results, resulting in the wind speed predicted by the model being higher than the measured values (Figure 6).

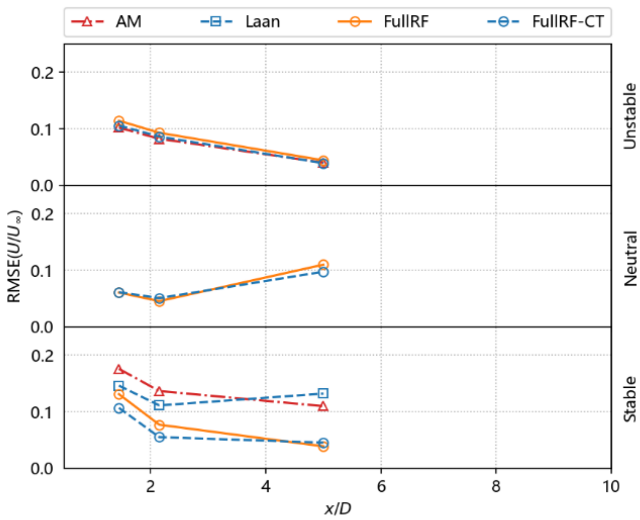

Figure 7. RSME of the wake deficit at hub height under the stable condition: "-CT" represents models using AD based on the thrust coefficient.

2.3. Effects of ground on wake expansion

Figure 8 depicts the distribution of wake wind speeds in the vertical cross-section of a wind turbine at various distances downstream under unstable, neutral, and stable atmospheric conditions. The dark line encircling the wake indicates the wake boundary, characterized by a wake deficit of 0.05. The illustration reveals varying degrees of downstream wake center displacement at the 10D position behind the turbine across different operating conditions. The displacement is most pronounced under unstable conditions, which feature high turbulence intensity. Under such conditions, wake expansion occurs more rapidly compared to scenarios with lower turbulence. Additionally, the interaction between the ground and the wake is enhanced under high turbulence. This will cause the wake's centerline to shift downward toward the ground in the far-wake region, and the linear expansion of the wake at hub height is suppressed. Further investigations are conducted in Section 4 to assess whether the wake maintains linear expansion under the influences of high turbulence and ground effects.

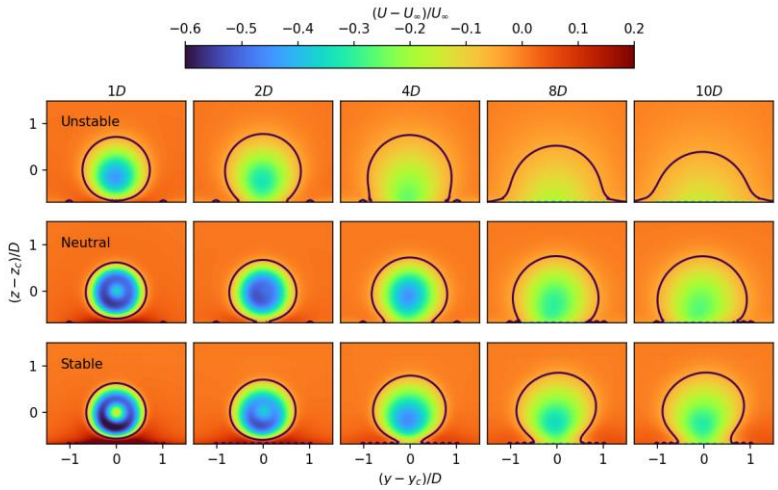

Figure 8. Cross-sectional diagram of wake deficits under different stability conditions.

3. Typical Engineering Wake Models with Linear Wake Expansion

3.1. A Modified Jensen Model Considering Atmospheric Stability Conditions

In the Jensen wake model [30], the wind speed deficit at distance x downstream of the rotor is calculated as follows:

$$\frac{\Delta U(x,r)}{U_\infty}=\frac{1-\sqrt{1-C_T}}{(1+2k_w x/D)^2} \tag{27}$$

where U_∞ is the inflow velocity, C_T is the thrust coefficient, k_w is the wake expansion rate and could be used to determine the wake boundary: at $r>D/2+k_w x$, $\Delta U(x)=0$ where $r=y-y_c$ represents the radial distance. In this paper, the coordinate of the wind turbine rotor's rotation center is set as the origin, i.e. $x_c=y_c=z_c=0$.

For wind turbine wakes in a neutral atmospheric boundary layer, the suggested values of k are 0.075 for onshore cases and 0.04 or 0.05 for offshore ones [31, 32]. To account for the influence of atmospheric stability on the wake, Peña et al. [33] related the wake expansion coefficient to incoming wind speed, friction velocity, and hub height:

$$k_w=u_*/U_H \tag{28}$$

$$u_*=\frac{U_H}{\displaystyle\int_{z_0}^{H}\frac{1}{z}\phi_m(\zeta)\mathrm{d}z} \tag{29}$$

where z_0 is the aerodynamic roughness length, H represents the hub height.

3.2. Guassian-shaped Wake Models

Because of the assumption of a top-hat distribution for wake deficit profiles, the modified Jensen model is not able to capture the radial dependence of the wake. In fact, the wake deficit has an approximately Gaussian symmetric shape after some downwind distances [1] . By applying conservation of mass and momentum, Bastankhah and Porté-Agel [34] suggested to replace the top-hat assumption with a Gaussian distribution for the wake deficit in the wake:

$$\frac{\Delta U(x,r)}{U_\infty}=\left[1-\sqrt{1-\frac{C_T}{8(\sigma/D)^2}}\right]\exp\left(-\frac{r^2}{2\sigma^2}\right) \tag{30}$$

where σ is the wake width.

As shown in various numerical and experimental studies on wind turbine wakes [34, 35], the wake width is approximately linear with x after some downstream distance:

$$\frac{\sigma}{D}=k^*\frac{x-x_0}{D}+\sigma_0\equiv k^*\frac{x}{D}+\sigma_R \tag{31}$$

in which $k^*\equiv\partial\sigma/\partial x$ represents the wake expansion coefficient corresponding to the Gaussian distribution wake model and x_0 characterizes the near-wake length, defined as the axial distance where the wind speed deficit exhibits a Gaussian distribution-like profile. σ_R is the parameter equivalent to the wake width at (x = 0) as assumed in the Gaussian wake profile model. Since the wind speed deficit at the rotor varies from the Gaussian distribution, k^* is often considered a linear function of the longitudinal turbulence intensity [34]. σ_R is then divided into two categories: one being a linear function of k^* [34] and the other related to k^*, as well as the near-wake length x_0 [36]:

$$\sigma_R=-\frac{x_0}{D}k^*+\sigma_0 \tag{32}$$

Bastankhah et al. [36] divided the wake of a wind turbine into three regions: the near-wake core region, the outer atmospheric free-flow region, and the boundary layer region between them (Figure 9). They derived a formula for calculating by relating the growth rate of the boundary layer thickness to the turbulence intensity and the difference in wind speeds inside and outside the wake. The formula is as follows:

$$\frac{x_0}{D}=\frac{1+\sqrt{1-C_T}}{\sqrt{2}[\alpha_* I_n+\beta_*(1-\sqrt{1-C_T})]} \tag{33}$$

with $\beta_*=0.154$ and α_* is typically set to 2.32 in wind tunnel experiments. Based on the analysis of field wake observations by Fuertes et al. [37], the near-wake length x_0 of wind turbines in wind farms is observed to be smaller than the values observed in wind tunnels under equivalent turbulence intensity and thrust coefficient conditions. Therefore, in wind farms, α_* is typically set to the value recommended by Fuertes et al. [37], which is 3.6. $\sigma_0=1/\sqrt{8}$ for unyawed conditions.

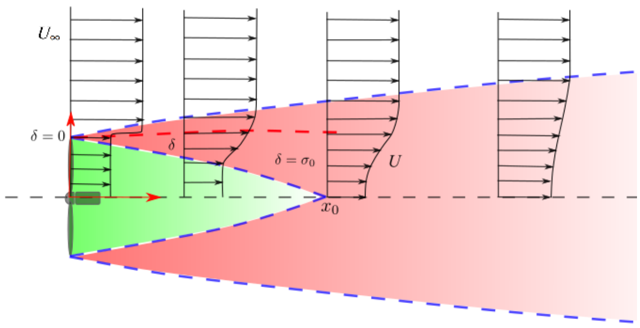

Figure 9. Schematic overview of wind turbine near-wake and far-wake regions.

Turbulence plays a significant role in the evolution of wind turbine wakes and is generally considered to have a linear relationship with the wake expansion coefficient k^*. This study introduces three typical Gaussian wake models: the Fuertes model [37], Cheng model [8], and Campagnolo model [38] (Table 2). These models are compared with the engineering model proposed in this study for predicting wind turbine wake wind speeds under different atmospheric stability conditions.

Table 2. Typical Gaussian wake models, where I_u and I_v is longitudinal turbulence intensity and lateral turbulence intensity, respectively.

Model	Fuertes	Cheng	Campagnolo
Scale	The experimental measurement of the nacelle lidar	Considering lateral turbulence	Wind tunnel experiment
k^*	$0.35I_u$	$0.223I_v+0.022$	$0.089I_u+0.027$
σ_R	$-1.91k^*+0.34$		Equation(32), $\alpha_*=0.952$, $\beta_*=0.262$

3.3. Estimation of the Streamwise Turbulence Intensity at Hub Height

To assess the prediction accuracy of the model, this study first utilizes existing measurements of longitudinal turbulence intensity. If such measurements are unavailable, a proposed similarity function is employed for estimation. Based on the similarity function σ_u/u_* at a height of 70m:

$$I_u \equiv \frac{\sigma_u}{U_H} = \frac{2.24\left(1+b_0\zeta\right)^{1/2}}{\displaystyle\int_{z_0}^{H} \kappa z \phi_m(\zeta)\,\mathrm{d}z} \tag{34}$$

the FullRF similarity function is employed for ϕ_m, with b_0 set to 0.4 and -0.5 for stable and unstable conditions, respectively.

The lateral turbulence intensity is estimated using the method recommended in the ESDU [39]:

$$I_v = \left[1-0.22\cos^4\left(\frac{\pi H}{2h_{\mathrm{ABL}}}\right)\right] I_u \tag{35}$$

in which $h_{\mathrm{ABL}} = u_*/(12\Omega\sin\phi)$ represents the boundary layer height, $\Omega=72.9\times10^{-6}$ rad/s denotes the Earth's rotational angular velocity, and ϕ represents the local latitude.

4. The Proposed Engineering Wake Expansion Model

Atmospheric stability significantly influences the dynamics of wind turbine wakes by affecting turbulence intensity. Consequently, this study delineates the impact of atmospheric stability by establishing a correlation between turbulence intensity and the wake expansion coefficient. Equation (32) provides a method for estimating the wake expansion width based on the length of the near wake. This study predominantly utilizes numerical simulations to construct the model under high turbulence scenarios. Furthermore, under stable conditions, classical similarity functions often overpredict the vertical gradients of wind speed and underpredict the incoming turbulence intensity [16]. To address these discrepancies, the chapter uses similarity functions, adjusted based on measured data from a wind farm in China, to simulate wake effects. The simulation results are then used to create a data training set and a validation set, which are employed to develop an engineering wake model that takes atmospheric stability into account. For specific details, refer to Figure 10.

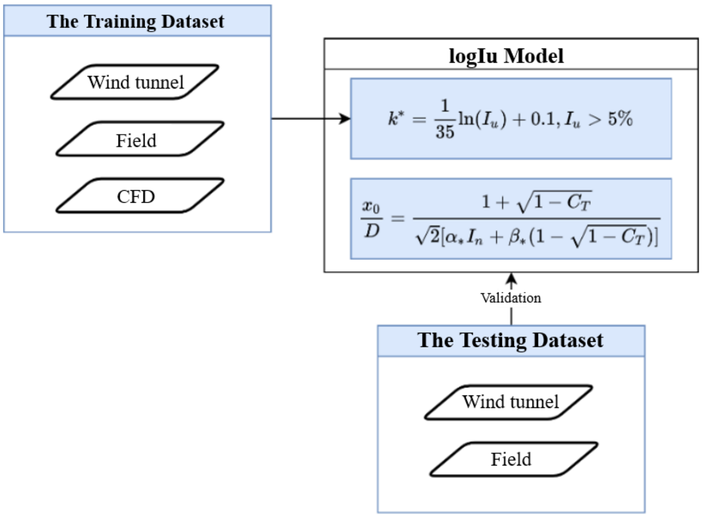

Figure 10. Workflow for training and testing the logIu model.

4.1. Wake Model Development Data Set

The dataset consists of two parts: training data used to fit the correlation between k^* and I_u, and testing data used to validate the reliability of the developed wake model. The dataset description is shown in Table 3. The dataset includes wind speed data from the wake region of 13 types of wind turbines, obtained through wind tunnel experiments, field measurements, and numerical simulations, along with relevant inflow information. The shaded sections in the table indicate cases that involve non-neutral operating conditions. The cases are primarily matched with the name of the wind turbine, and when the turbine name is unknown, they correspond to the author and publication date of the data source. The subclass denotes the presence of multiple operating environments or conditions for the same wind turbine, where TSR represents the Tip Speed Ratio. The three stability levels indicate the presence of neutral, unstable, and stable operating environments. In the subclass, LES stands for Large Eddy Simulation, with inflow conditions set based on the Businger-Dyer similarity functions, considering the influence of the atmospheric boundary layer thickness. The effect of the atmospheric boundary layer thickness is confirmed by applying a pressure gradient within the computational domain to ensure that the Reynolds stress decreases to zero at the top of the atmospheric layer. RANS refers to Reynolds-Averaged Navier-Stokes simulations using the FullRF turbulence model to simulate wind turbine wakes.

Table 3. Basic information of the wake dataset.

Experiment type	Cases	Subcases	D(m)	H(m)	Wake Range (D)
Wind tunnel tests	Dou2019 [40, 41]	TSR=4,5,6	0.2	0.75	4.5~10
	WiRE-01[42]		0.15	0.125	4~10
	Ruland-913[43]	In turbulent flows	0.9	1.12	2.5~8.5
	G1[38]	Three offshore cases	1.1	0.83	5~10
	Hancock2014 [2, 44, 45]	Neutral, unstable and stable cases	0.416	0.3	3~10
Field experiments	Nibe-B [46, 47]	C_T=0.67,0.77,0.82	40	45	2.5~7.5
	Liberty C96 [37]		96	80	0.6~10
	Vestas V80-2MW [9]	Neutral (LES)：4 types of z_0 and three	80	70	3~15

		stability classes (LES)			
	Danwin [48-50] Nordtank [5]	Neutral：C_T=0.65,0.82 Non-neutral (Experiments+RANS)	23	35	4.2~9.6
	Haizhuang [4]	Three stability classes (Experiments +RANS)	41	36	2~5
	Nibe-B [46, 47]		93	67	1.45,2.15,5

The wind turbine operating conditions corresponding to wind tunnel experiments are as follows: (1) A two-bladed wind turbine in the Dou 2019 case [40, 41], operating at different tip-speed ratios (TSR=4, 5, 6), pitch angles, and yaw angles. (2) A model wind turbine (WiRE-01) with a diameter of 15 cm, operating at the optimum tip-speed ratio ($\lambda_{opt} \approx 3.8$), corresponding to a thrust coefficient $C_T \approx 0.78$ [42]. (3) A six-bladed Rutland 913 model wind turbine operating under turbulent conditions ($I_u = 14.5\%$) [43]. (4) The G1 turbine operates in two environments: one simulating offshore wind farm conditions with a turbulence intensity of 6.1% and the other simulating onshore wind farm conditions with a turbulence intensity of 11% [38]. (5) The Hancock 2014 case involves a three-bladed model wind turbine operating under neutral, stable, and unstable conditions [2, 44, 45].

For non-wind tunnel experiments, the Vestas V80-2MW wind turbine only has wake results from LES results[9], while other turbines have field-measured data. Turbines with observed wake data and operating conditions include: (1) A 40m diameter three-bladed Nibe-B 630kW wind turbine operating at 33 rpm [46, 47]. (2) The 2.5MW Liberty C96 wind turbine with a thrust coefficient of approximately 0.82, capable of measuring wake wind speeds from 0.6 to 10 rotor diameters using a laser radar mounted on the nacelle [37]. (3) The three-bladed Danwin 180kW wind turbine operating under different atmospheric thermal stability conditions [48-50]. (4) The actively stalled 500kW Nordtank wind turbine equipped with a pulsed laser radar mounted on the nacelle, capable of measuring wake wind speeds behind the rotor at different atmospheric stability conditions [5]. (5) The Haizhuang 2MW wind turbine, with wind measurement towers installed on both the north and south sides and related wind turbine SCADA operational data, providing wind speed data at positions 1.45*D*, 2.15*D*, and 5*D* behind the rotor under various stability conditions [4]. Table 4 provides supplementary parameters for the wake simulation cases of wind turbines, with the wake expansion coefficient obtained through least squares fitting of numerical simulation data.

Table 4. Supplementary wind turbine wake simulation cases.

Turbine	z_0(m)	L(m)	u*(m)	I_u(%)	k*(10-3)
Haizhuang	5×10^{-8}	∞	0.114	3.6	5.79
	5×10^{-6}		0.146	4.7	6.28
	5×10^{-5}		0.17	5.4	8.07
	0.05	-100	0.382	16.2	37.47
		-1000	0.5122	17.4	44.05
	0.5	-100	0.601	25.6	69.38
		-50	0.655	31.6	70.13
		-20	0.755	45	83.43
Nordtank	0.2	∞	0.542	14.6	51.26
Danwin	5×10^{-4}	35	0.198	4.5	3.23

4.1.1 The Training Dataset

Table 5 presents turbulence intensity and thrust coefficients for the training data. The turbulence intensity provided in the training data ranges from 1.6% to 45%. Given that LES numerical results from Vestas wind turbines frequently informed the development of wake models, these simulations have also been incorporated into the training dataset for this study [51-53].

Table 5. The hub-height turbulence intensity and thrust coefficient of wind turbine.

Training Cases		I_u(%)	C_T
Wind tunnel experiments	Dou2019(TSR=4)	1	0.85
	G1: offshore	6.1	0.79,0.73,0.68
	Rutland-913	14.5	0.94
Field measurement	Nibe-B	11	0.77,0.82
	Liberty C96	1.6~17	0.82
LES numerical simulation	Vestas: neutral	4.8~13.4	0.8
	Vestas: three stability classes	6.5~10	0.8
RANS numerical simulation	Haizhuang	3.6~44.7	0.84
	Nordtank	6.1~18.3	0.83
	Danwin	4.5~10	0.82

4.1.2 Validation data

Apart from the training data, other cases will be employed to verify the accuracy and reliability of the proposed model in predicting wind turbine wakes. The inflow conditions and thrust coefficients for these validation cases are listed in Table 6.

Table 6. The inflow information and thrust coefficient of wind turbine for the validation case.

Case validation		U_∞	L(m)	I_u (%)	C_T
Wind tunnel	Dou2019(TSR=5,6)	6	∞	1	0.91,0.94
	WIRE-01	5	∞	7	
	Hancock2014	2.3,2.3,1.47	0.956, ∞ ,-1.26	8.5,6.6,5.3	0.42,0.48,0.48
Field	Nibe-B	11.52	∞	10.5	0.67
	Danwin	8,11,8	-50,∞ ,90.6	9.7,6,7.6	0.82,0.65,0.82
	Nordtank	6.82,7.03,6.76	-84.8,∞,29	14,15,10	0.71,0.75,0.83

4.2. The logIu Engineering Wake Model

The relationship between the wake expansion coefficient k^* and the longitudinal turbulence intensity I_u obtained from the training data is shown in Figure 11. The training data suggests a proportional relationship between the wake expansion coefficient and the longitudinal turbulence when the longitudinal turbulence intensity is below 10%. Beyond this threshold, the rate of change of the wake expansion coefficient diminishes with increasing turbulence intensity. In light of supplementary RANS numerical simulations, the Fuertes model significantly overestimates the wake expansion coefficient k^* at $I_u > 15\%$. Based on this finding, a logarithmic relationship is proposed and updated as formalized in Equation (36) in this study. The newly developed engineering wake model, termed "logIu", incorporates this logarithmic relationship, with "Iu" denoting the model's dependence of the model on longitudinal turbulence intensity.

$$k^* = \begin{cases} 0.014, & I_u \leq 5\% \\ \dfrac{1}{35}\ln(I_u) + 0.1, & I_u > 5\% \end{cases} \tag{36}$$

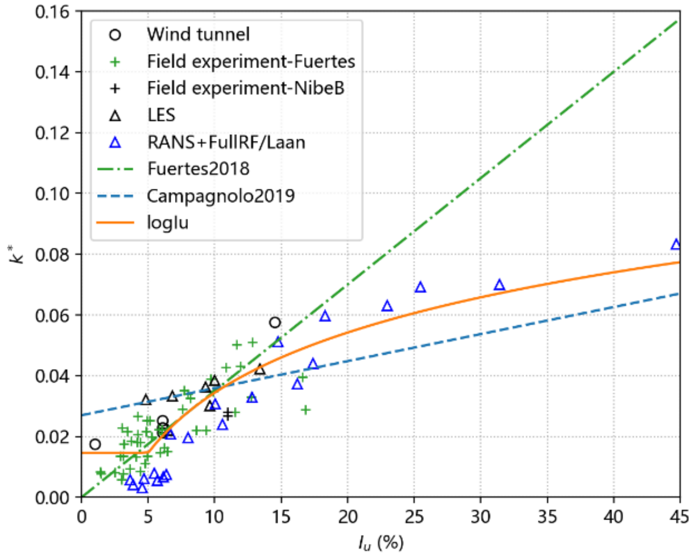

Figure 11. The relationship and fitting curve between k* and Iu from different data sources. The training data for the Fuertes2018 model [37] comes from a nacelle-mounted lidar wake measurement experiment and the Campagnolo2019 model [38] also defines the wake expansion coefficient as a linear function of the streamwise turbulence intensity.

The nonlinear relationship between the wake expansion coefficient and longitudinal turbulence intensity is influenced by the proximity to the ground or sea surface. As the wake expands downstream, it may interact with the ground, producing a compressive effect on the expanding wake. This interaction can increase wind speeds near the ground while decreasing them at hub height, effectively diminishing the wake expansion coefficient. At lower turbulence intensities (<12%), the wake expansion coefficient and range are minimal, resulting in weaker compressive effects from the ground. Thus, the wake expansion coefficient increases linearly with an increase in longitudinal turbulence intensity. However, once turbulence intensity surpasses a critical threshold (12%), the ground's compressive effect becomes pronounced, inhibiting the linear growth of the wake expansion coefficient with turbulence intensity.

5. Validation and Evaluation of the logIu wake expansion model

5.1. Wind Tunnel Experiment Validation

Figure 12 compares the measured wind speeds at hub height under neutral conditions in a wind tunnel against predictions from various engineering models. Specifically, Figure 12 delineates the wind speeds along the wake centerline at $TSR = 5, 6$ for the Dou2019 case. The proposed model shows better agreements with the experiment than other models. The Campagnolo model, which is formulated based on wind tunnel wake measurement data, tends to underestimate wake wind speeds at $x > 4D$. Similarly, other wake models also show varying degrees of underestimation, with the Jensen model displaying a notably significant deviation. For identical wake widths, the Jensen model distributes the wind speed reduction uniformly across the wake, leading to an overestimation of speeds near the wake centerline and an underestimation at the edges of the wake width.

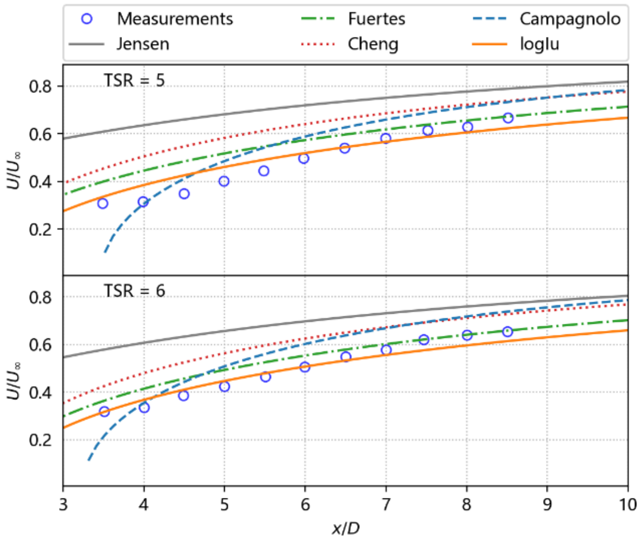

Figure 12. Wake model prediction of the relative velocity on the wake centerline of Dou2019 case.

The prediction accuracy of the wake speed for WiRE-01 of the proposed model is also higher than those of other models (Figure 13). Relative to the logIu model, the Campagnolo model significantly overestimated the wind speed loss at $x = 4D$ by approximately 37% near the wake centerline. In contrast, other models predict lower wake deficits near the wake center, with the Cheng model showing the most substantial underestimation. In this verification case, the longitudinal turbulence intensity of the hub height is I_u = 7%. However, according to the original method described in the Cheng model's literature, it is only 5.6%. This discrepancy suggests that the Cheng model underestimates wake deficits when using a lower turbulence intensity. Meanwhile, the predictions by the Fuertes model fall between those of the logIu and Cheng models: Fuertes model utilizes a larger a_* than logIu model in wind tunnel scenarios, resulting in a smaller calculated near-wake length and a faster predicted wake recovery, whereas the Cheng model employs a higher turbulence intensity, leading to a quicker wake recovery rate than that of Fuertes.

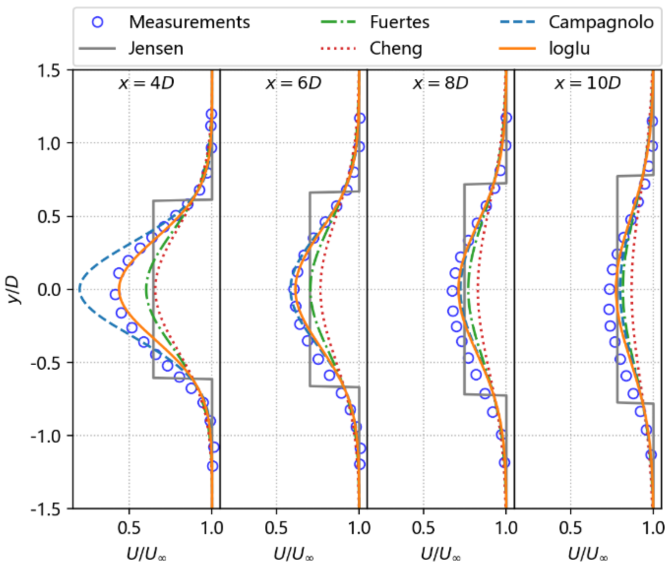

Figure 13. Wake model prediction of the relative velocity on the wakes of WiRE-01 case.

Figure 14 shows the predicted versus actual wind speeds for various models under different atmospheric conditions. The wake measurement data from the Hancock 2014 study highlights the influence of atmospheric stability on wind turbine wakes: at $x = 10D$ the maximum wake deficit is only 15% under unstable conditions, whereas it is 25% under stable conditions. Among the models, the logIu model demonstrates the highest accuracy in predicting wakes. Under non-neutral conditions, the Campagnolo model tends to overestimate wake deficits, failing to deliver accurate predictions at $x = 2 \sim 5D$. This indicates that despite being optimized with wind tunnel data and performing adequately under neutral conditions, the Campagnolo model lacks satisfactory prediction capability for wind turbine wakes under non-neutral conditions. Similar to neutral conditions, the Jensen, Fuertes, and Cheng models markedly underestimate wake deficits, especially in the near-wake region and under stable atmospheric conditions.

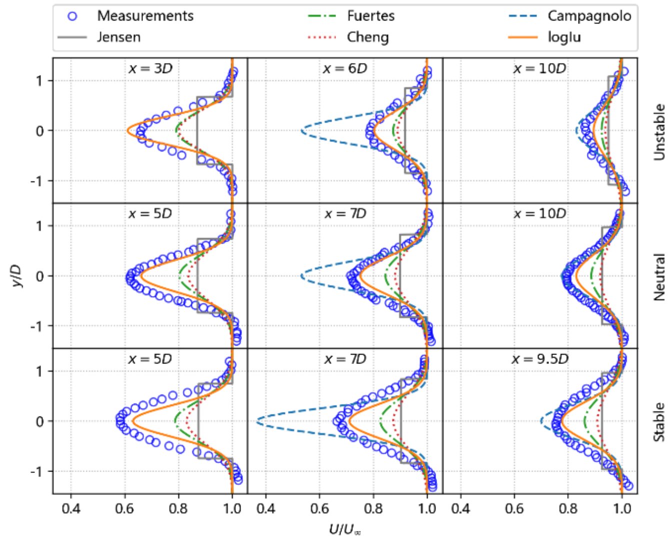

Figure 14. Wake wind speed predictions at hub height from different models for the Hancock2014 case.

5.2. Field Observation Experiment Validation

5.2.1 Neutral Conditions

Figure 15 evaluates the wake velocity models against measurement data at locations $x = 2.5D$, $5.5D$, and $8D$ for the Nibe B wind turbine under neutral conditions. The results reveal that the wind speeds predicted by the logIu model align most closely with the actual measurements. The accuracy of the Fuertes and Cheng models are slightly less precise than that of logIu, although the discrepancy is not marked. The Jensen model still underestimates the wake deficits at the wake center ($y \approx 0$) and overestimating it at the wake edge ($y \approx 0.5D$). Because the parameter $\alpha_* = 0.952$ in the Campagnolo model is optimized through wind tunnel tests and is much smaller than the recommended value 3.6 for actual wind farms, the Campagnolo model predicts a higher value for x_0 and thus overestimates wake deficits.

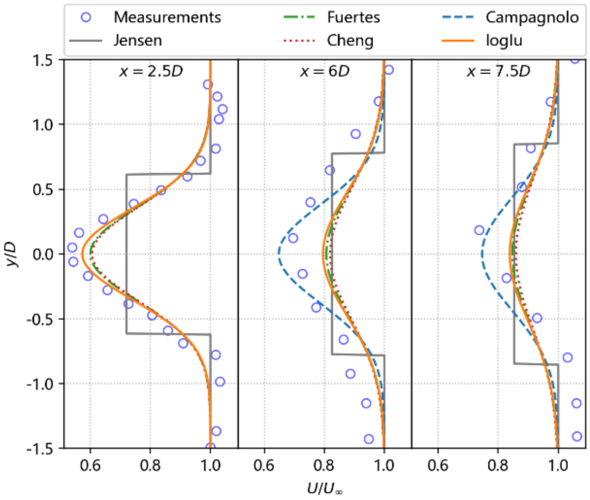

Figure 15. Wake wind speed predictions at hub height from different models for the Nibe-B wind turbine.

5.2.2 Non-neutral Conditions

Figure 16 compares the model-predicted wind speeds under different stability conditions with four wind turbine field measurement values. Overall, aside from overestimating the wind speed loss near the wake center under strong unstable conditions ($x=5D$) and strong stable conditions ($x=2D$), the logIu model generally offers reliable predictions across different atmospheric stabilities. The Fuertes and Cheng models exhibit a slightly lower overall predictive accuracy than logIu, with a more pronounced discrepancy evident in the Danwin scenario. The "top-hat" shape of the Jensen model still exhibits poor accuracy in predicting wakes in the near-wake region (up to 35% at $2\sim2.5D$) and overestimates wake deficits at $y=0.5D$. In contrast, the Campagnolo model significantly overestimates wake deficits in these cases, with overestimation ratios reaching up to 170% at $x=3D$ and 30% to 40% at $x=6.1D$, illustrating substantial predictive errors in actual wind farm applications.

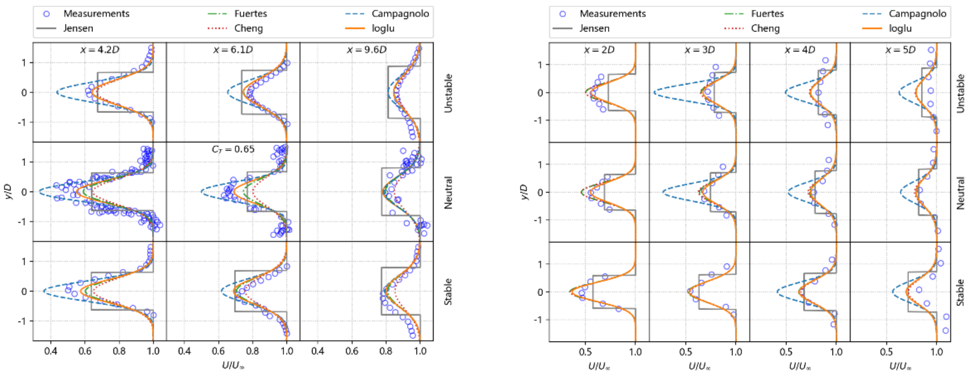

(a) (b)

Figure 16. The wake wind speed predictions at hub height from different models: (a) Danwin; (b) Nordtank.

5.3. Overall Model Evaluation

Figure 17 compares the RMSE (U/U_∞) values for various models across different operational environments. The wake velocities predicted by the logIu and Campagnolo models are closer to the measured values of wind turbine wakes in the wind tunnel compared to the predictions of other engineering models. The RMSE values for logIu and Campagnolo models range from 0.04 to 0.06, which is substantially lower than the 0.07 to

0.09 range observed for alternative models. The prediction accuracy of logIu exhibits a slight decline in actual wind farms, with the corresponding RMSE increasing from approximately 0.04 in the wind tunnel to 0.063. This value remains marginally lower than the 0.07 RMSE associated with Fuertes's model. The decrease in prediction accuracy may be attributed to the increased complexity of operational environments in real wind farms and potential limitations in measurement instrumentation precision. The prediction accuracy of Fuertes and logIu in actual wind farms are similar because the functional relationships between the wake expansion coefficient and turbulence intensity for the two models demonstrate convergence at $5\% \leqslant I_u \leqslant 12\%$. The prediction accuracy of the Cheng model is slightly lower than that of the Fuertes model, but both are higher than that of the Jensen model considering atmospheric stability. For all cases, logIu has the highest accuracy in wake prediction, followed by the Fuertes and Campagnolo models, with the Jensen model exhibiting the lowest accuracy in wake velocity predictions.

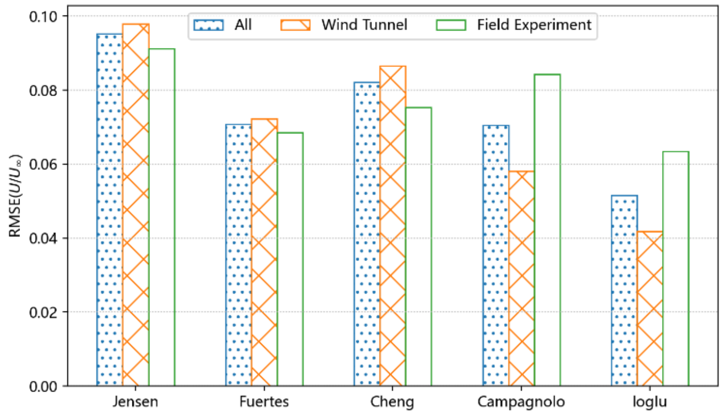

Figure 17. The RMSE(U/U∞) of each model corresponding to different operating environments.

The RMSE (U/U_∞) values of various models under different atmospheric stability conditions are shown in Figure 18. The logIu model demonstrates the lowest RMSE across all examined stability conditions, indicating superior overall prediction accuracy. Except for Campagnolo, the reliability of investigated models in predicting wake velocities generally decreases with increasing stability. In both wind tunnel simulations and real atmospheric boundary layer conditions, increasing stability is associated with a decrease in the boundary layer height. This phenomenon allows wind turbines to exceed the surface layer, where the Reynolds stresses are relatively constant. Above the surface layer, the Reynolds stresses diminish with increasing height, resulting in more pronounced disparities in the turbulence intensity between the upper and lower sections of the wind turbine rotor sweep area. The models studied in this study assume that the relative wind speed loss is symmetrically distributed along the wake centerline, which is not conducive to capturing the increasing difference in turbulence intensity between the upper and lower parts of the rotor sweep area as the stability increases. This limitation in the underlying assumptions of the models may contribute to the observed decrease in predictive accuracy under conditions of heightened atmospheric stability.

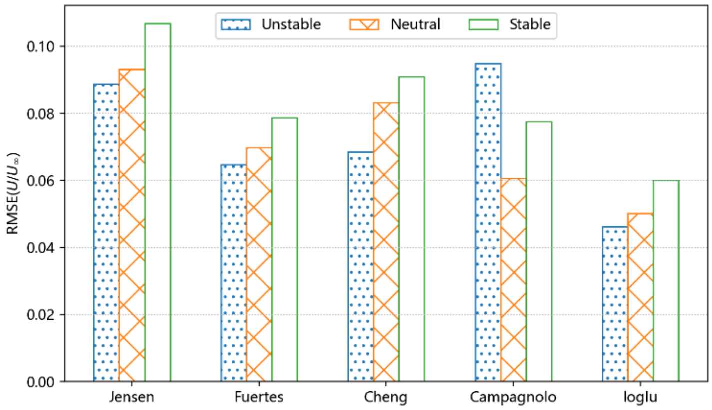

Figure 18. The RMSE (U/U∞) of each model under different stability conditions.

6. Conclusion

This study examines the influence of ground effects on wake expansion and proposes a novel nonlinear wake expansion model that incorporates both atmospheric stability and ground effects. The proposed model is calibrated using extensive datasets comprising wake measurements from wind-tunnel experiments, field observations, and numerical simulations. A comparative analysis is conducted between the wake wind speeds predicted by the proposed model and those of other typical models. The principal findings of this study are summarized as follows.

(1) Ground effects tend to suppress wake expansion at far-wake locations, and this suppression becomes more pronounced under high turbulence. This ground-wake interaction at far-wake locations, particularly under high turbulence intensity, has the potential to induce a downward displacement of the wake centroid and thus suppress wake expansion at the hub height.

(2) The experimental data and simulation results indicate that the previously assumed linear relationship between the wake expansion coefficient and turbulence intensity is invalid at high turbulence levels. Instead, the wake expansion coefficient exhibits a logarithmic relationship with longitudinal turbulence intensity.

(3) The proposed logIu model demonstrates superior overall accuracy in predicting wake wind speeds, with corresponding RMSE values ranging from 0.04 to 0.063. The prediction accuracy of the wake wind speeds across various models generally exhibits an inverse relationship with increasing atmospheric stability. This trend suggests that wake prediction is the most challenging task under stable atmospheric conditions.

These findings contribute to the advancement of wake modeling techniques and provide valuable insights into the complex interactions among atmospheric conditions, ground effects, and wake behavior in wind energy applications.

Author Contributions: Conceptualization, X. X. H. and C. X.; methodology, T. G. W. and X.D. M.; software, J.M. Z. and Z. C.; validation, S. F. F. and F. F. X.; formal analysis, Z. C.; investigation, S. F. F.; resources, J. M. Z.; data curation, J. M. Z.; writing—original draft preparation, X. X. H.; writing—review and editing, J. M. Z. and X. D. M.; visualization, X. X. H.; supervision, C. X.; project administration, F. F. X.; funding acquisition, X. X. H. All authors have read and agreed to the published version of the manuscript.

Funding: This research was funded by the National Natural Science Foundation of China, grant number 52106238, the Fundamental Research Funds for the Central Universities (Grant No. B230201051) and Royal Society International Exchanges under Grant IEC\NSFC\223091.

Conflicts of Interest: The authors declare no conflicts of interest.

References

1. Chamorro, L.P. and F. Port-Agel, *Effects of Thermal Stability and Incoming Boundary-Layer Flow Characteristics on Wind-Turbine Wakes: A Wind-Tunnel Study.* Boundary-Layer Meteorology, 2010. **136**(3): p. 515-533.
2. Hancock, P.E. and F. Pascheke, *Wind-tunnel simulation of the wake of a large wind turbine in a stable boundary layer: Part 2, the wake flow.* Boundary-layer meteorology, 2014. **151**(1): p. 23-37.
3. Zhang, W., C.D. Markfort, and F. Port-Agel, *Wind-turbine wakes in a convective boundary layer: A wind-tunnel study.* Boundary-layer meteorology, 2013. **146**(2): p. 161-179.
4. Han, X., et al., *Atmospheric stability and topography effects on wind turbine performance and wake properties in complex terrain.* Renewable energy, 2018. **126**: p. 640-651.
5. Machefaux, E., et al., *An experimental and numerical study of the atmospheric stability impact on wind turbine wakes.* Wind Energy, 2016. **19**(10): p. 1785-1805.
6. Foreman, R.J., B. Cañadillas, and N. Robinson, *The Atmospheric Stability Dependence of Far Wakes on the Power Output of Downstream Wind Farms.* Energies, 2024. **17**(2): p. 488.
7. Peña, A., P.-E. Réthoré, and O. Rathmann, *Modeling large offshore wind farms under different atmospheric stability regimes with the Park wake model.* Renewable Energy, 2014. **70**: p. 164-171.
8. Cheng, Y., et al., *A new analytical model for wind turbine wakes based on Monin-Obukhov similarity theory.* Applied Energy, 2019. **239**: p. 96-106.
9. Wu, Y.-T. and F. Port-Agel, *Atmospheric turbulence effects on wind-turbine wakes: An LES study.* energies, 2012. **5**(12): p. 5340-5362.
10. Abkar, M. and F. Port-Agel, *Influence of Atmospheric Stability on Wind-Turbine Wakes: A Large-Eddy Simulation Study.* Physics of Fluids, 2015. **27**(3): p. 035104.
11. Gao, X., et al., *Investigation and validation of 3D wake model for horizontal-axis wind turbines based on filed measurements.* Applied Energy, 2020. **260**: p. 114272.
12. Huanqiang, Z., et al., *Investigation of a new 3D wake model of offshore floating wind turbines subjected to the coupling effects of wind and wave.* Applied Energy, 2024. **365**: p. 123189.
13. Ling, Z., et al., *A three-dimensional wake model for wind turbines based on a polynomial distribution of wake velocity.* Ocean Engineering, 2023. **282**: p. 115064.
14. Wang, Z. and X. Yang, *Upward Shift of Wind Turbine Wakes in Large Wind Farms.* Energies, 2023. **16**(24): p. 8051.
15. Chamorro, L.P. and F. Porté-Agel, *A Wind-Tunnel Investigation of Wind-Turbine Wakes: Boundary-Layer Turbulence Effects.* Boundary-Layer Meteorology, 2009. **132**(1): p. 129-149.
16. Han, X., et al., *Monin–Obukhov Similarity Theory for Modeling of Wind Turbine Wakes under Atmospheric Stable Conditions: Breakdown and Modifications.* Applied Sciences, 2019. **9**(20): p. 4256.
17. Drela, M., *XFOIL: An analysis and design system for low Reynolds number airfoils*, in *Low Reynolds number aerodynamics*. 1989, Springer: Berlin. p. 1-12.
18. Du, Z. and M. Selig. *A 3-D stall-delay model for horizontal axis wind turbine performance prediction*. in *1998 ASME Wind Energy Symposium*. 1998. Reno,NV,U.S.A.: Reno,NV,U.S.A.
19. Shen, W.Z., W.J. Zhu, and J.N. Sørensen, *Actuator line/Navier–Stokes computations for the MEXICO rotor: Comparison with detailed measurements.* Wind Energy, 2012. **15**(5): p. 811-825.
20. Shen, W.Z., et al., *Tip loss corrections for wind turbine computations.* Wind Energy, 2005. **8**(4): p. 457-475.
21. Alinot, C. and C. Masson, *$k-$ Model for the Atmospheric Boundary Layer Under Various Thermal Stratifications.* Journal of Solar Energy Engineering, 2005. **127**(4): p. 438-443.
22. van der Laan, M.P., M.C. Kelly, and N.N. Srensen, *A new k-epsilon model consistent with Monin--Obukhov similarity theory.* Wind Energy, 2017. **20**(3): p. 479-489.
23. Temel, O. and J. van Beeck, *Two-equation eddy viscosity models based on the Monin-Obukhov similarity theory.* Applied Mathematical Modelling, 2017. **42**: p. 1-16.
24. Chang, C.-Y., et al., *A consistent steady state CFD simulation method for stratified atmospheric boundary layer flows.* Journal of Wind Engineering and Industrial Aerodynamics, 2018. **172**: p. 55-67.
25. Businger, J.A., et al., *Flux-profile relationships in the atmospheric surface layer.* Journal of the atmospheric Sciences, 1971. **28**(2): p. 181-189.
26. Dyer, A.J., *A review of flux-profile relationships.* Boundary-Layer Meteorology, 1974. **7**(3): p. 363-372.
27. Zhang, X., *CFD simulation of neutral ABL flows*. 2009.
28. Sørensen, J.N., et al., *Simulation of wind turbine wakes using the actuator line technique.* Philosophical Transactions of the Royal Society A: Mathematical, Physical and Engineering Sciences, 2015. **373**(2035): p. 20140071.

29. Weller, H.G., et al., *A tensorial approach to computational continuum mechanics using object-oriented techniques.* Computers in Physics, 1998. **12**(6): p. 620-631.
30. Jensen, N.O., *A note on wind generator interaction*. 1983, Roskilde, Denmark: Ris{\o} National Laboratory.
31. Barthelmie, R.J., et al., *Modelling and measuring flow and wind turbine wakes in large wind farms offshore.* Wind Energy, 2009. **12**(5): p. 431-444.
32. Gmen, T., et al., *Wind turbine wake models developed at the technical university of Denmark: A review.* Renewable and Sustainable Energy Reviews, 2016. **60**: p. 752-769.
33. Peña, A., P.E. Réthoré, and M.P. van der Laan, *On the application of the Jensen wake model using a turbulence-dependent wake decay coefficient: the Sexbierum case.* Wind Energy, 2016. **19**(4): p. 763-776.
34. Bastankhah, M. and F. Port-Agel, *A new analytical model for wind-turbine wakes.* Renewable Energy, 2014. **70**: p. 116-123.
35. Johnson, P.B., et al. *On the spread and decay of wind turbine wakes in ambient turbulence*. in *Journal of Physics: Conference Series*. 2014. Bristol (UK): IOP Publishing.
36. Bastankhah, M. and F. Port-Agel, *Experimental and theoretical study of wind turbine wakes in yawed conditions.* Journal of Fluid Mechanics, 2016. **806**: p. 506-541.
37. Carbajo Fuertes, F., C. Markfort, and F. Port-Agel, *Wind turbine wake characterization with nacelle-mounted wind lidars for analytical wake model validation.* Remote Sensing, 2018. **10**(5): p. 668.
38. Campagnolo, F., et al. *Comparison of Analytical Wake Models with Wind Tunnel Data*. in *Journal of Physics: Conference Series*. 2019. Bristol (UK): IOP Publishing.
39. Lawson, T.V. and others, *ESDU 85020 Characteristics of atmospheric turbulence near the ground. Part II: single point data for strong winds (neutral atmosphere)*. 2001.
40. Dou, B., et al., *Experimental investigation of the performance and wake effect of a small-scale wind turbine in a wind tunnel.* Energy, 2019. **166**: p. 819-833.
41. Dou, B., et al., *Wake model for horizontal-axis wind and hydrokinetic turbines in yawed conditions.* Applied energy, 2019. **242**: p. 1383-1395.
42. Bastankhah, M. and F. Port-Agel, *A new miniature wind turbine for wind tunnel experiments. Part ii: Wake structure and flow dynamics.* Energies, 2017. **10**(7): p. 923.
43. Chu, C.-R. and P.-H. Chiang, *Turbulence effects on the wake flow and power production of a horizontal-axis wind turbine.* Journal of Wind Engineering and Industrial Aerodynamics, 2014. **124**: p. 82-89.
44. Hancock, P.E. and S. Zhang, *A wind-tunnel simulation of the wake of a large wind turbine in a weakly unstable boundary layer.* Boundary-Layer Meteorology, 2015. **156**(3): p. 395-413.
45. Hancock, P.E., et al., *Wind Tunnel Simulation of a Wind Turbine Wake in Neutral, Stable and Unstable Wind Flow.* Journal of Physics: Conference Series, 2014. **555**(1): p. 012047.
46. Pederson, B.M. and P. Nielson. *Description of the two Danish 630kW wind turbines, Nibe-A and Nibe-B, and some preliminary test results, DEFU, Denmark*. in *Third International Symposium on Wind Energy Systems*. 1980. Copenhagen, Denmark: BHRA Fluid Engineering.
47. Taylor, G.J., *Wake measurements on the Nibe wind-turbines in Denmark*. 1990, Leatherhead (UK): National Power, Technology and Environment Centre.
48. Magnusson, M., K.G. Rados, and S.G. Voutsinas, *A study of the flow downstream of a wind turbine using measurements and simulations.* Wind Engineering, 1996: p. 389-403.
49. Magnusson, M. and A.-S. Smedman, *Influence of atmospheric stability on wind turbine wakes.* Wind Engineering, 1994: p. 139-152.
50. Magnusson, M. and A.-S. Smedman, *Air flow behind wind turbines.* Journal of Wind Engineering and Industrial Aerodynamics, 1999. **80**(1-2): p. 169-189.
51. Niayifar, A. and F. Porté-Agel, *Analytical modeling of wind farms: A new approach for power prediction.* Energies, 2016. **9**(9): p. 741.
52. Ishihara, T. and G. Qian, *A New Gaussian-Based Analytical Wake Model for Wind Turbines Considering Ambient Turbulence Intensities and Thrust Coefficient Effects.* Journal of Wind Engineering and Industrial Aerodynamics, 2018. **177**.
53. Ge, M., et al., *A two-dimensional model based on the expansion of physical wake boundary for wind-turbine wakes.* Applied energy, 2019. **233**: p. 975-984.